



## Self-supported ternary $(\text{Ni}_x\text{Fe}_y)_2\text{P}$ nanoplates arrays as an efficient bifunctional electrocatalyst for overall water splitting

Shuaishuai Li <sup>a</sup>, Xing Wang <sup>a</sup>, Min Li <sup>a</sup>, Jian Liu <sup>a</sup>, Chaorong Li <sup>a</sup>, Huaping Wu <sup>b</sup>, Daoyou Guo <sup>a</sup>, Fangmin Ye <sup>a</sup>, Shunli Wang <sup>a</sup>, Lin Cheng <sup>a</sup>, Aiping Liu <sup>a,c,d,\*</sup>

<sup>a</sup> Center for Optoelectronics Materials and Devices, Key Laboratory of Optical Field Manipulation of Zhejiang Province, Department of Physics, Zhejiang Sci-Tech University, Hangzhou, 310018, PR China

<sup>b</sup> Key Laboratory of E&M, Ministry of Education & Zhejiang Province, Zhejiang University of Technology, Hangzhou, 310014, PR China

<sup>c</sup> State Key Laboratory of Structural Analysis for Industrial Equipment, Dalian University of Technology, Dalian, 116024, PR China

<sup>d</sup> State Key Laboratory of Digital Manufacturing Equipment and Technology, Huazhong University of Science and Technology, Wuhan, 430074, PR China



### ARTICLE INFO

#### Article history:

Received 8 March 2019

Received in revised form

4 June 2019

Accepted 5 July 2019

Available online 6 July 2019

#### Keywords:

Ternary transition metal phosphides

Self supporting

Bifunctional electrocatalyst

Overall water splitting

Synergistic effect

### ABSTRACT

Developing non-precious metal bifunctional electrocatalysts for effective overall water splitting is promising to realize high-efficient renewable energy production. In this work, ternary  $(\text{Ni}_x\text{Fe}_y)_2\text{P}$  nanoplates arrays on 3D self-supported nickel foams were prepared through a simple coelectrodeposition followed by phosphorization. The synthesized  $(\text{Ni}_x\text{Fe}_y)_2\text{P}$  nanoplates arrays showed remarkable bifunctional electrocatalytic performances in the KOH electrolyte, with the Tafel slopes of  $57.8 \text{ mV}\cdot\text{dec}^{-1}$  and  $53.6 \text{ mV}\cdot\text{dec}^{-1}$ , and low overpotentials of  $115 \text{ mV}$  and  $182 \text{ mV}$  to reach a current density of  $10 \text{ mA cm}^{-2}$  for hydrogen evolution reaction and oxygen evolution reaction, respectively. In addition, the optimized  $(\text{Ni}_{0.66}\text{Fe}_{0.33})_2\text{P}$  anode and cathode demonstrated outstanding ability for overall water splitting in the two-electrode alkaline electrolyzer, generating a current density of  $10 \text{ mA cm}^{-2}$  at the applied cell voltage of  $1.61 \text{ V}$ . This benefited by the active surface to expedite reactants absorption, faster electron transport in the solid-liquid interface and reduced charge-transfer resistance due to the bimetallic synergistic effect. This delicate design of bifunctional transition metal phosphides provides a potential approach to realize water reuse and energy regeneration by the full water splitting.

© 2019 Elsevier Ltd. All rights reserved.

## 1. Introduction

With the increasing demand for energy and the continuous exploitation of non-fossil fuels, the development of technologies for clean and sustainable energy production has been given great attention [1,2]. Especially, the electrochemical water splitting is recognized as one of the most promising technologies to generate hydrogen which could replace fossil fuels in the near future [3–6]. Though various high-efficient noble metals catalysts have been designed to overcome the sluggish kinetic barriers of hydrogen evolution reaction (HER) and oxygen evolution reaction (OER), and reduce the applied voltage of water splitting reaction, the challenges remain in terms of their relative high price, scarce resource

and complicated preparation technology [7–9]. It's comforting that some transition metal compounds, such as sulfides [10–14], selenides [14–16], carbides [17,18], nitrides [19], and oxides (or hydroxides) [20–23] are regarded as desired substitute for noble metal catalyst for HER [10–13,15,17–20,23] or OER [16,18,19,21,22] due to their relatively low adsorption free energy for proton or reactive oxygen species [24]. However, most well-developed HER catalysts lack efficient catalytic activity and stability in alkaline conditions [25]. Thus, it is particularly significant to develop high-efficient and low-cost bifunctional electrocatalysts for overall water splitting in the same electrolyte.

Recently, transition metal phosphides (TMPs) have been attracted considerable interest due to proven outstanding catalytic activity for HER and OER in alkaline conditions [26–34]. Numerous efforts have been devoted to designing nanostructures with more edge sites and chemical components with multivariate coupling [26–30]. For example, T. Liu et al. reported enhanced electrochemical HER activity of Mn doped CoP nanosheets arrays at all pH values due to the more thermo-neutral hydrogen adsorption free

\* Corresponding author. Center for Optoelectronics Materials and Devices, Key Laboratory of Optical Field Manipulation of Zhejiang Province, Department of Physics, Zhejiang Sci-Tech University, Hangzhou, 310018, PR China.

E-mail address: [liuiping1979@gmail.com](mailto:liuiping1979@gmail.com) (A. Liu).

energy ( $\Delta G_{H^*}$ ) [26]. M. Wu et al. prepared hybrid NiP<sub>2</sub>/NiO nanorod arrays for efficient HER in alkaline environments in terms of the facilitated adsorption of hydrogen intermediates at negatively charged P species [27]. J. Chang et al. conformed the advanced OER activity of oxidized cobalt phosphide (CoP) nanorods in alkaline conditions via the forming a CoP@CoOx core-shell structure [28]. M. Ledendecker et al. proved the bifunctional electrocatalysis of nanostructured Ni<sub>5</sub>P<sub>4</sub> films for full water splitting in alkaline environment due to the enhanced interaction between reaction intermediates and Ni<sub>5</sub>P<sub>4</sub> films by the proton acceptor and hydride acceptor sites [29]. G. Read et al. exhibited excellent electrocatalytic HER and OER performances of TMPs films by the reaction of metal foils (Fe, Co, Ni, Cu, and NiFe) and various organophosphine reagents [30]. Compared to binary TMPs, the design of ternary components is more feasible strategy to improve intrinsic catalytic activity and enhance the overall catalytic performance and durability by means of the synergistic effect of mixed metals, which can push the  $\Delta G_{H^*}$  to an intermediate value and facilitate the transfer of electrons and charges [31–34]. However, the study of ternary components interaction with hydrogen atoms and reactive oxygen species in the overall water electrolysis is limited [35–39] and the improvement of bifunctional catalytic performance is still urgent.

Accordingly, we investigate the bifunctional electrocatalytic behavior of ternary (Ni<sub>x</sub>Fe<sub>y</sub>)<sub>2</sub>P nanoplates arrays on 3D self-supported nickel foams (NFs) via low-temperature phosphorization of their layered double hydroxide (LDH) precursor (Ni<sub>x</sub>Fe<sub>y</sub>-LDH). The element selection of Ni and Fe is based on the adjustable  $\Delta G_{H^*}$  of Ni<sub>2</sub>P and Fe<sub>2</sub>P and possible further optimization [31,33]. The as-obtained (Ni<sub>x</sub>Fe<sub>y</sub>)<sub>2</sub>P nanoplates with appropriate Ni/Fe atomic ratio (2:1) exhibit extremely high catalytic activity and excellent durability in alkaline solutions with the HER overpotential of 115 mV to achieve a current density of 10 mA cm<sup>-2</sup> and a low Tafel slope of 57.8 mV·dec<sup>-1</sup>, and the OER overpotential of only 182 mV to reach a current density of 10 mA cm<sup>-2</sup> and a low Tafel slope of 53.6 mV·dec<sup>-1</sup>. The overpotentials are satisfactory when compared to the reported ones of most active bifunctional electrocatalysts, indicating the potential of (Ni<sub>x</sub>Fe<sub>y</sub>)<sub>2</sub>P nanoplates arrays as a promising electrocatalyst for overall water splitting.

## 2. Experimental section

### 2.1. Chemicals and materials

All of the chemicals used in the experiments were of analytical grade and used without further purification. Commercial NFs with

the thickness of 1.5 mm were obtained from Suzhou Taili material technology co. Ltd. Nickel(II) nitrate hexahydrate (Ni(NO<sub>3</sub>)<sub>2</sub>·6H<sub>2</sub>O, 98%, Aladdin), iron(II) sulfate heptahydrate (FeSO<sub>4</sub>·7H<sub>2</sub>O, ≥99%, Aladdin), hydrochloric acid (HCl), acetone (CH<sub>3</sub>COCH<sub>3</sub>), ethanol (C<sub>2</sub>H<sub>6</sub>O) and sodium hypophosphite (NaH<sub>2</sub>PO<sub>2</sub>) were purchased from Hangzhou Mike Chemical Instrument Co. Ltd. Deionized (DI) water obtained from pure water equipment system (BK-10C, 18.2 MΩ cm) was used for solution preparation.

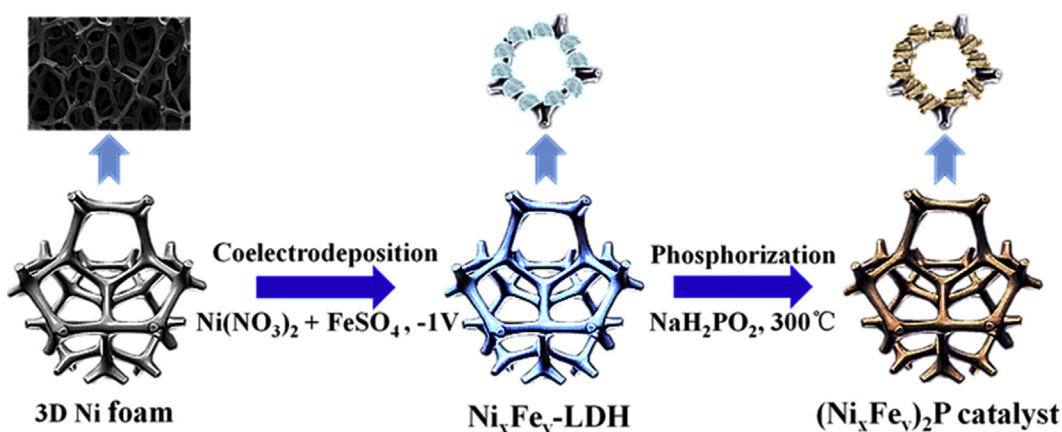
### 2.2. Fabrication of (Ni<sub>x</sub>Fe<sub>y</sub>)<sub>2</sub>P nanoplates arrays on 3D nickel foam

A piece of NF (1 cm × 1.2 cm) was rinsed alternately with the HCl solution (2 M), acetone, ethanol and water to remove the NiO layer on the surface before use. When the NF was immersed into the mixed solution of Ni(NO<sub>3</sub>)<sub>2</sub> and FeSO<sub>4</sub>, the coelectrodeposition of Ni<sup>2+</sup> and Fe<sup>2+</sup> on the NF surface was carried out at -1 V (vs. Ag/AgCl) for 7 min via the three-electrode system including NF working electrode, platinum plate counter electrode and saturated Ag/AgCl reference electrode, generating the Ni<sub>x</sub>Fe<sub>y</sub>-LDH precursor. Then, the Ni<sub>x</sub>Fe<sub>y</sub>-LDH/NF was phosphorized at 300 °C for 2 h in a tube furnace with NaH<sub>2</sub>PO<sub>2</sub> (0.5 g) as the P source under N<sub>2</sub> atmosphere, obtaining the ternary (Ni<sub>x</sub>Fe<sub>y</sub>)<sub>2</sub>P catalyst (Scheme 1). By controlling the molar concentration ratio of Ni(NO<sub>3</sub>)<sub>2</sub> to FeSO<sub>4</sub> (1, 2 and 3) in the mixed solution (0.1 M), the bimetallic components in the (Ni<sub>x</sub>Fe<sub>y</sub>)<sub>2</sub>P catalysts was designed adjusted. The binary Ni<sub>2</sub>P and Fe<sub>2</sub>P references were fabricated by using the solution without FeSO<sub>4</sub> or Ni(NO<sub>3</sub>)<sub>2</sub>.

### 2.3. Structure and performance characterization

The crystalline structures of all as-prepared samples were identified by an X-ray powder diffractometer (XRD, Bruker AXS D8, Cu K $\alpha$  radiation with  $\lambda = 0.15418$  nm) with a velocity of 5°·min<sup>-1</sup> in the 2 $\theta$  range from 10 to 80°. The morphologies, components and microstructural features of the samples were obtained using a field emission scanning electron microscopy (FESEM, Hitachi S-4800) equipped with an energy-dispersive X-ray spectroscopy (EDS) at an accelerating voltage of 3 kV and a transmission electron microscopy (TEM, FEI Tecnai G2 F20). High-resolution TEM (HRTEM) images were obtained at an operating voltage of 300 kV. X-ray photoelectron spectroscopy (XPS) was collected by a Kratos' Axis Ultra DLD (delay line detector) photoelectron spectrometer with the binding energy calibrated by C1s as reference energy (C 1s = 284.6 eV).

The electrochemical performances of samples were performed by using a CHI 760E electrochemical workstation (CH Instruments,



**Scheme 1.** Schematic illustration for the synthesis of (Ni<sub>x</sub>Fe<sub>y</sub>)<sub>2</sub>P catalysts.

China) in 1 M KOH solution at room temperature with the platinum wire as counter electrode and a saturated calomel electrode (SCE) as reference electrode. All potentials were calibrated to reversible hydrogen electrode (RHE) based on the equation ( $E_{\text{RHE}} = E_{\text{Hg}/\text{HgCl}} + 0.241 + 0.0591 \times \text{pH}$ ). All data were iR compensated. The HER and OER performances of catalysts were acquired in 1 M KOH solution by the linear sweep voltammetry (LSV) at a scanning rate of 5 mV s<sup>-1</sup>. To evaluate the electrochemical active surface of materials, the cyclic voltammetry (CV) measurements were performed at different scan rates of 10, 20, 30, 40 and 50 mV s<sup>-1</sup> in the potential range between 0.1 and 0.2 V, and then the double layer capacitance ( $C_{\text{dl}}$ ) and the real electrochemical surface area ( $\text{ECSA} = C_{\text{dl}}/C_s$ ,  $C_s$  was the specific capacitance in an alkaline electrolyte and equal to 0.040 mF cm<sup>-2</sup>) were determined [10]. Electrochemical impedance spectroscopy (EIS) measurement was carried out in the overpotential of 200 mV using a frequency range between 10<sup>5</sup> Hz and 0.01 Hz with the amplitude of 5 mV. The HER durability of catalytic electrode was tested at a static overpotential of -120 mV for 24 h. The electrode endurance of OER was conducted at constant current densities of 10 mA cm<sup>-2</sup>. The quantities

of generated H<sub>2</sub> and O<sub>2</sub> during overall water electrolysis were confirmed every 20 min by using a Techcomp GC 7900 gas chromatograph.

### 3. Results and discussion

#### 3.1. Morphology and microstructure of $(\text{Ni}_x\text{Fe}_y)_2\text{P}$ catalysts

Fig. 1(a) shows the XRD patterns of different samples. The three peaks at 44.5°, 51.8° and 76.4° are assigned to the (002), (100) and (110) crystal planes of NF (PDF#04-0850), respectively. The peaks at 40.8°, 47.3°, 54.2°, 54.9° and 74.7° for Ni<sub>2</sub>P are assigned to the (111), (210), (300), (211) and (400) plans of Ni<sub>2</sub>P (PDF#03-0953), respectively. The peaks at 40.4°, 47.3°, 54.1°, 54.6° and 74.6° for Fe<sub>2</sub>P are corresponding to the (111), (210), (300), (211) and (400) plans of Fe<sub>2</sub>P (PDF#51-094), respectively. After the coelectroposition of Ni and Fe on NF, the diffraction peaks at 37.3° and 64.1° for Ni<sub>x</sub>Fe<sub>y</sub>-LDH are indexed to (002) crystal plane of NiOOH (PDF#06-0141) and (002) one of FeOOH (PDF#18-0639), respectively. The EDS results show that the atomic ratios of Ni/Fe in the Ni<sub>x</sub>Fe<sub>y</sub>-LDH or (Ni<sub>x</sub>Fe<sub>y</sub>)<sub>2</sub>P

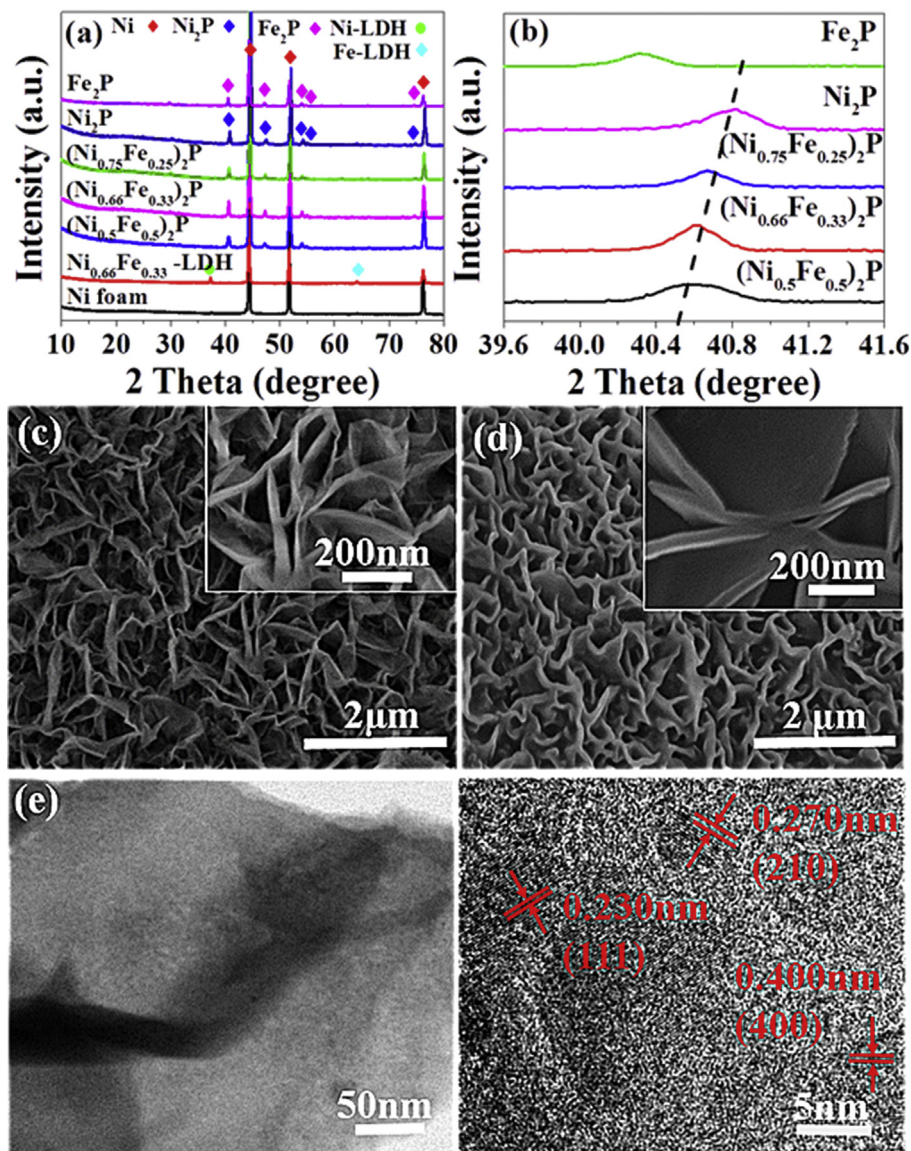


Fig. 1. (a,b) XRD patterns of different samples. (c,d) SEM images of (c)  $\text{Ni}_{0.66}\text{Fe}_{0.33}$ -LDH and (d)  $(\text{Ni}_{0.66}\text{Fe}_{0.33})_2\text{P}$  catalyst. (e) TEM and (f) HRTEM images of  $(\text{Ni}_{0.66}\text{Fe}_{0.33})_2\text{P}$  catalysts.

samples are about 1:1, 2:1 and 3:1 when the molar concentration ratio of  $\text{Ni}(\text{NO}_3)_2$  to  $\text{FeSO}_4$  in the mixed solution was set to 1, 2 and 3, respectively (Fig. S1). Therefore, we correspondingly define the samples with  $(\text{Ni}_{0.5}\text{Fe}_{0.5})_2\text{P}$ ,  $(\text{Ni}_{0.66}\text{Fe}_{0.33})_2\text{P}$  and  $(\text{Ni}_{0.75}\text{Fe}_{0.25})_2\text{P}$ , respectively. After  $\text{Ni}_x\text{Fe}_y$ -LDH phosphorization, the  $(\text{Ni}_x\text{Fe}_y)_2\text{P}$  still retain the hexagonal phosphide structure of  $\text{Ni}_2\text{P}$  and  $\text{Fe}_2\text{P}$  [31,40]. Furthermore, the lattice constants of  $(\text{Ni}_x\text{Fe}_y)_2\text{P}$  are closely related to the Ni/Fe atomic ratios (Fig. 1(b)) and decrease with the increasing Fe component in the composites due to the substitution of Ni by Fe with a smaller atomic radius [37]. This is also the result of synergistic effect of binary metals during crystallization. Fig. 1(c and d) displays the morphologies of  $\text{Ni}_x\text{Fe}_y$ -LDH and  $(\text{Ni}_x\text{Fe}_y)_2\text{P}$  samples. All composites show similar structures with the average width of nanoplates arrays of about 500 nm and thickness of about 50 nm on the NF. The TEM image in Fig. 1(e) also confirms the nanosheet morphology of  $(\text{Ni}_{0.66}\text{Fe}_{0.33})_2\text{P}$  electrocatalyst. The well-resolved lattice fringes of  $(\text{Ni}_{0.66}\text{Fe}_{0.33})_2\text{P}$  electrocatalyst with interplanar distances of 0.230, 0.270 and 0.400 nm are in good agreement with the interlayers of (111), (210) and (400) planes, respectively (Fig. 1(f)). Notice that the interplanar distances are slightly larger than those of hexagonal  $\text{Ni}_2\text{P}$  (0.226, 0.260 and 0.390 nm). The might be due to the substitution of Ni by Fe in the ternary  $\text{Ni}_x\text{Fe}_y$  phosphide [37,41].

The XPS spectra were further obtained to illustrate the chemical states of different elements in  $(\text{Ni}_{0.66}\text{Fe}_{0.33})_2\text{P}$  nanoplates. The XPS survey spectrum in Fig. 2(a) confirms the presence of Ni, Fe and P elements. In the high-resolution Ni 2p spectrum in Fig. 2(b), the peaks located at about 853.3 eV and 869.8 eV are assigned to the  $\text{Ni}^{\delta+}$  ( $0 < \delta < 2$ ) in the Ni-P bond [38,42]. The binding energies of 857.0 eV and 875.5 eV with two satellite peaks at 862.7 eV and 881.0 eV can be attributed to the oxidized Ni species (nickel oxide) on the sample surface [38,42,43]. The peaks at 706.9 eV and 721.0 eV in the Fe 2p<sub>3/2</sub> and Fe 2p<sub>1/2</sub> (Fig. 2(c)) correspond to the

formation of Fe-P [36,38,44], with their satellites located at 711.0 eV and 724.3 eV corresponding to the oxidized Fe on the catalyst surface [36,44,45]. The two peaks at 129.3 eV and 130.3 eV in the high-resolution P 2p region are assigned to P 2p<sub>1/2</sub> and P 2p<sub>3/2</sub> (Fig. 2(d)) [42,44], respectively, due to the formation of metal phosphides.

### 3.2. Electrocatalytic performances of hydrogen evolution reaction and oxygen evolution reaction for $(\text{Ni}_x\text{Fe}_y)_2\text{P}$ catalysts

The HER electrocatalytic activity of  $(\text{Ni}_x\text{Fe}_y)_2\text{P}$  catalysts with different Ni/Fe ratios were studied in 1 M KOH via a typical three-electrode system. From the LSV curves in Fig. 3(a), the  $(\text{Ni}_{0.66}\text{Fe}_{0.33})_2\text{P}$  catalyst presents the best HER performance with relative small overpotentials of 115, 151 and 210 mV to reach HER current densities of 10, 20 and 50  $\text{mA cm}^{-2}$ , respectively. Additionally, the overpotential of  $(\text{Ni}_{0.66}\text{Fe}_{0.33})_2\text{P}$  catalyst to obtain the HER current density of 10  $\text{mA cm}^{-2}$  is lower 15, 20, 19 and 58 mV than those of  $\text{Ni}_2\text{P}$ ,  $(\text{Ni}_{0.75}\text{Fe}_{0.25})_2\text{P}$ ,  $(\text{Ni}_{0.5}\text{Fe}_{0.5})_2\text{P}$  and  $\text{Fe}_2\text{P}$ , respectively (Fig. 3(c)). The Tafel plot is further provided to prove the excellent HER catalytic activity of  $(\text{Ni}_{0.66}\text{Fe}_{0.33})_2\text{P}$  catalyst. A small Tafel slope usually leads to a greatly enhanced HER rate at a moderate increase of overpotential [46–48]. As shown in Fig. 3(b), the Tafel slope of  $(\text{Ni}_{0.66}\text{Fe}_{0.33})_2\text{P}$  catalyst is 57.8  $\text{mV dec}^{-1}$ , indicating a Volmer-Heyrovsky mechanism for the HER process at  $(\text{Ni}_{0.66}\text{Fe}_{0.33})_2\text{P}$  surface and the Heyrovsky step reaction as the rate determining step [49,50]. In particular, this Tafel slope is relatively low when compared to many recently reported catalysts (Table S1 in Supporting Information). In order to explore the effect mechanism of Ni/Fe ratios on the HER activity of  $(\text{Ni}_x\text{Fe}_y)_2\text{P}$  catalysts, the EIS measurement was performed for electrode kinetic analysis during the HER process. As shown in Fig. 3(d), the low Ohmic series resistance of the system ( $R_s$ , about 3–5  $\Omega$ ), the intercept of

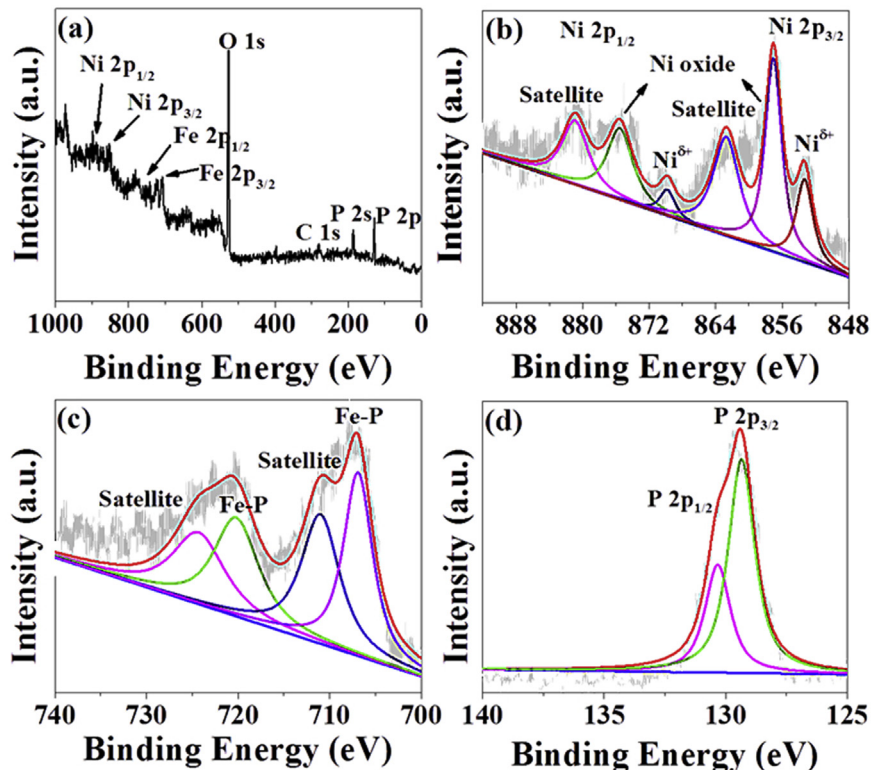
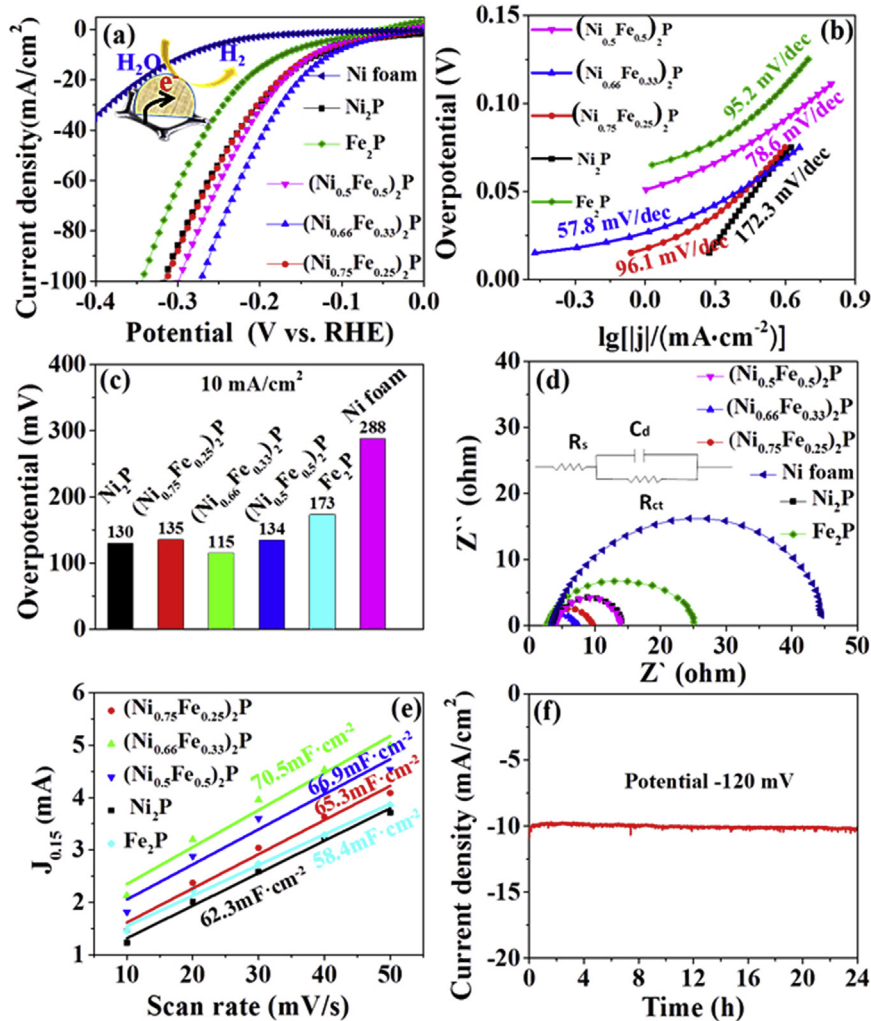


Fig. 2. (a) XPS survey spectrum of  $(\text{Ni}_{0.66}\text{Fe}_{0.33})_2\text{P}$ ; high-resolution spectra of Ni 2p (b), Fe 2p (c) and P 2p (d) for  $(\text{Ni}_{0.66}\text{Fe}_{0.33})_2\text{P}$ .



**Fig. 3.** Hydrogen evolution reaction at various electrodes in 1 M KOH: (a) LSV curves, (b) corresponding Tafel slopes, (c) overpotentials obtained at the current density of 10 mA cm<sup>-2</sup>, (d) Nyquist plots at an overpotential of 200 mV (vs. RHE), (e) the relations of difference between anodic and cathodic currents at 0.15 V (vs. RHE) with scan rate, (f) time dependence of the current density for (Ni<sub>0.66</sub>Fe<sub>0.33</sub>)<sub>2</sub>P at a static overpotential of -120 mV for 24 h.

semicircle and real axis, indicates excellent conductivity of electrolyte [12]. The Nyquist semicircle diameter for (Ni<sub>0.66</sub>Fe<sub>0.33</sub>)<sub>2</sub>P catalyst is much smaller than those of other samples, suggesting the lowest charge transfer resistance ( $R_{ct}$ ) between the solid-liquid interface and highest reaction kinetic. Additionally, the double-layer capacitance ( $C_{dl}$ ) was obtained by the scanning area of CV cures at the Non-Faraday region (Fig. S2) and the ECSA was calculated to estimate the intrinsic electrochemical activity of the catalysts. As shown in Fig. 3(e), the (Ni<sub>0.66</sub>Fe<sub>0.33</sub>)<sub>2</sub>P has the biggest  $C_{dl}$ , demonstrating the most catalytic active sites exposed to electrolyte during the HER process. When the LSV curves are normalized to ECSA, the (Ni<sub>0.66</sub>Fe<sub>0.33</sub>)<sub>2</sub>P has still the highest catalytic activity for HER (Fig. S3a), demonstrating its wonderful intrinsic electrochemical activity. The (Ni<sub>0.66</sub>Fe<sub>0.33</sub>)<sub>2</sub>P catalyst also exhibits excellent stability over a 24 h long-term test at a static overpotential of -120 mV (vs. RHE) (Fig. 3(f)) without obvious change in the morphology, crystalline structure and surface chemical state (Fig. S4). In brief, such superior HER activity for (Ni<sub>0.66</sub>Fe<sub>0.33</sub>)<sub>2</sub>P catalyst with preferred Ni/Fe ratio could be rationalized as the appropriate synergistic effect of Ni and Fe in the composite [39], which not only provides more active surface to expedite the absorption of reactants but also facilitates the electron transfer in the

solid-liquid interface and reduces charge-transfer resistance. Thus, the Ni/Fe ratio in the ternary phosphides plays a key factor in improving the HER activity and optimizing the performance of HER catalyst.

In a same way, the outstanding OER electrocatalytic activity of (Ni<sub>0.66</sub>Fe<sub>0.33</sub>)<sub>2</sub>P catalyst was also confirmed in 1 M KOH with the typical three-electrode system. Fig. 4(a) and Fig. S3(b) demonstrate the LSV curves of different catalysts at a scan rate of 5 mV s<sup>-1</sup>. The Ni<sub>2</sub>P catalyst shows a distinct anodic peak around 1.4 V due to the change in the Ni oxidation state from Ni<sup>2+</sup> to Ni<sup>3+</sup> [51,52]. Furthermore, with the incorporation of Fe in the (Ni<sub>x</sub>Fe<sub>y</sub>)<sub>2</sub>P, the potential of Ni(OH)<sub>2</sub>/NiOOH oxidation peak shifts more higher, indicating that the Fe incorporation can suppress the electrochemical oxidation reaction from Ni<sup>2+</sup> to Ni<sup>3+</sup>. This could be attributed to the change of redox properties of Ni in the presence of Fe with the obvious decrease in oxidation peak area [37,52]. The (Ni<sub>0.66</sub>Fe<sub>0.33</sub>)<sub>2</sub>P catalyst exhibits the highest OER activity under alkaline condition and produces catalytic current densities of 10, 50, and 100 mA cm<sup>-2</sup> at a series overpotentials of 182, 280, and 325 mV, respectively. In contrast, Ni<sub>2</sub>P, Fe<sub>2</sub>P, (Ni<sub>0.5</sub>Fe<sub>0.5</sub>)<sub>2</sub>P, and (Ni<sub>0.75</sub>Fe<sub>0.25</sub>)<sub>2</sub>P require the overpotentials of 246, 215, 209, and 206 mV to obtain the current density of 10 mA cm<sup>-2</sup>, respectively

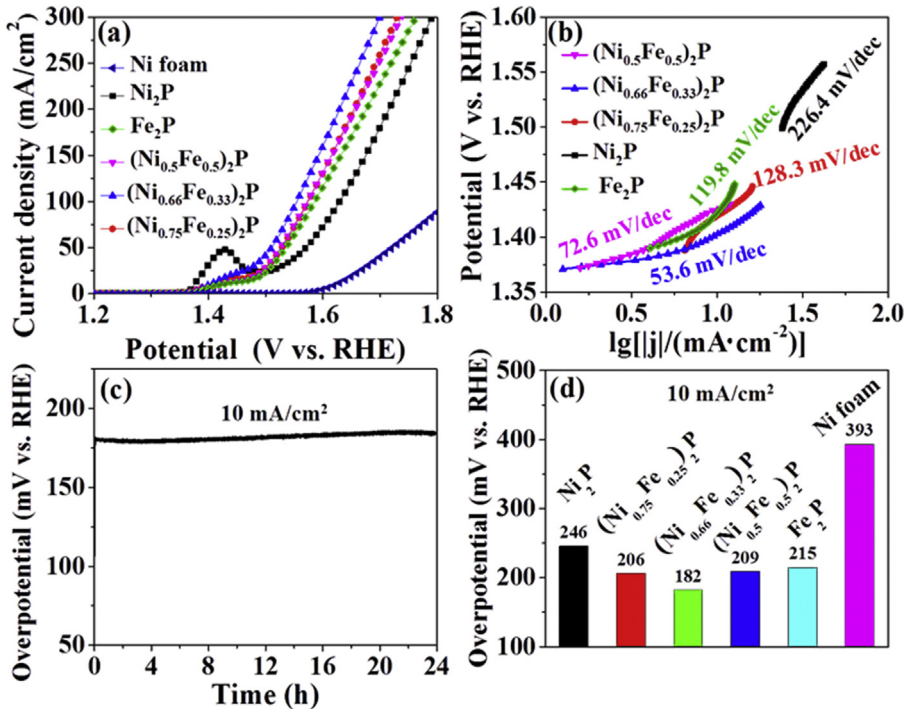


**Fig. 4.** Oxygen evolution reaction at various electrodes in 1 M KOH: (a) LSV curves, (b) the corresponding Tafel plots, (c) the long-term stability of  $(\text{Ni}_{0.66}\text{Fe}_{0.33})_2\text{P}$  at a constant current density of  $10 \text{ mA cm}^{-2}$ , (d) the overpotentials obtained at  $10 \text{ mA cm}^{-2}$  by the constant-current test.

(Fig. 4(c-d)). Therefore, Fe introduction increases the electrocatalytic reaction kinetics of OER due to the modification of electronic structure of the catalytic active center after Fe incorporation [39]. The Tafel plot of  $(\text{Ni}_{0.66}\text{Fe}_{0.33})_2\text{P}$  catalyst presents the smallest value of  $53.6 \text{ mV} \cdot \text{dec}^{-1}$  (Fig. 4(b)) when compared to  $\text{Ni}_2\text{P}$ ,  $(\text{Ni}_{0.75}\text{Fe}_{0.25})_2\text{P}$ ,  $(\text{Ni}_{0.5}\text{Fe}_{0.5})_2\text{P}$  and  $\text{Fe}_2\text{P}$  ( $226.4$ ,  $128.3$ ,  $72.6$  and  $119.8 \text{ mV} \cdot \text{dec}^{-1}$ , respectively). The overpotential at the current density  $10 \text{ mA cm}^{-2}$  for  $(\text{Ni}_{0.66}\text{Fe}_{0.33})_2\text{P}$  catalyst is lower than many reported ones of transition metal phosphide (Table S2). Therefore, the introduction of Fe is favorable for the improvement of OER reaction kinetics. The stability of  $(\text{Ni}_{0.66}\text{Fe}_{0.33})_2\text{P}$  catalyst was continuously tested by the chronopotentiometry for 24 h (Fig. 4(c)). The overpotential does not obviously change with the morphology and crystalline structure of  $(\text{Ni}_{0.66}\text{Fe}_{0.33})_2\text{P}$  catalyst well maintained after OER stability test (Figs. S5a–c). However, XPS results indicate

that the oxygen content of catalyst surface increases with an obvious decrease in the phosphorus content after OER test (Table S3). When the surface is sputtered by Ar plasma for about 2 min, the oxygen signal is weakened (Fig. S5). This means that the  $(\text{Ni}_{0.66}\text{Fe}_{0.33})_2\text{P}$  catalyst surface is partly oxidized during the OER process.

Based on the results mentioned above, the  $(\text{Ni}_{0.66}\text{Fe}_{0.33})_2\text{P}$  catalyst is identified as potential bifunctional electrocatalyst with excellent electrocatalytic activity and stability toward both HER and OER in alkaline electrolyte. Hence, we assembled an electrolyzer for overall water splitting with a two-electrode system by using a pair of  $(\text{Ni}_{0.66}\text{Fe}_{0.33})_2\text{P}$  nanoplates arrays on NFs as anode and cathode in 1 M KOH (Movie S1). From the polarization curve shown in Fig. 5(a), the current density of  $10 \text{ mA cm}^{-2}$  can be achieved at a cell voltage of  $1.61 \text{ V}$ . The result is comparable to most reported bifunctional

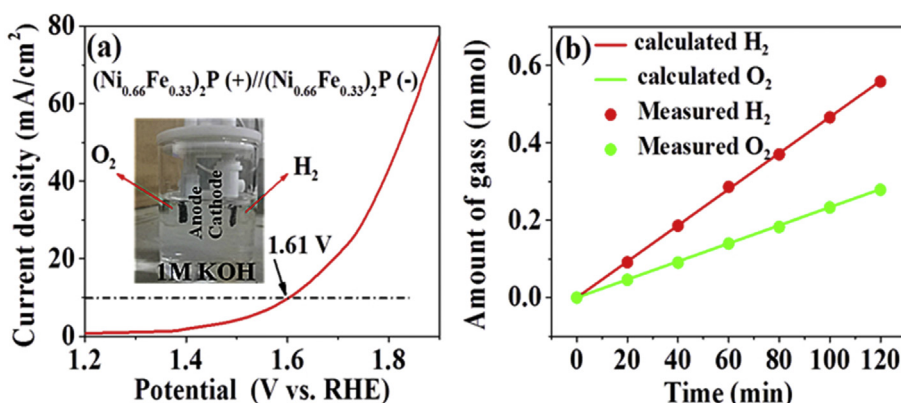


**Fig. 5.** (a) Polarization curve of the two-electrode water splitting system for the  $(\text{Ni}_{0.66}\text{Fe}_{0.33})_2\text{P}(+)/( \text{Ni}_{0.66}\text{Fe}_{0.33})_2\text{P}(-)$  in 1 M KOH at a scan rate of  $5 \text{ mV s}^{-1}$ , (the inset is the picture of assembled electrodes), (b)  $\text{H}_2$  and  $\text{O}_2$  amounts of the experimentally measured and the theoretically calculated versus time for overall water splitting by using  $(\text{Ni}_{0.66}\text{Fe}_{0.33})_2\text{P}$  in 1 M KOH at a constant current density of  $30 \text{ mA cm}^{-2}$ .

electrocatalysts for overall water splitting (**Table S4**). The generated H<sub>2</sub> and O<sub>2</sub> were further quantified by gas chromatography. The amounts of H<sub>2</sub> and O<sub>2</sub> from experimental measurement and theoretical calculation match well with the ratio of H<sub>2</sub> and O<sub>2</sub> closed to 2 (**Fig. 5(b)**), revealing the Faradaic efficiency of almost 100% for both HER and OER in 1 M KOH solution.

Supplementary data related to this article can be found at <https://doi.org/10.1016/j.electacta.2019.07.022>.

## 4. Conclusion

In summary, we have successfully synthesized ternary (Ni<sub>x</sub>Fe<sub>y</sub>)<sub>2</sub>P with nanoplates structures decorated on 3D self-supported nickel foam scaffolds through a facile coelectrodeposition method and subsequent low-temperature phosphorization process. Thanks to the unique 3D nanoplates structure and strong interactions among Ni, Fe and P, which can facilitate reactants absorption on catalysts, fasten electron transport in the solid-liquid interface and reduce ion-transfer resistance in electrolytes during the HER and OER processes. The optimized (Ni<sub>x</sub>Fe<sub>y</sub>)<sub>2</sub>P catalyst exhibits outstanding electrocatalytic performance as well as excellent long-term stability after 24 h toward both HER and OER in alkaline electrolyte, presenting the overpotential (current density of 10 mA cm<sup>-2</sup>) as low as 115 mV for HER with a small Tafel slope 57.8 mV·dec<sup>-1</sup> and 182 mV for OER with a small Tafel slope 53.6 mV·dec<sup>-1</sup>, respectively. Furthermore, the optimized (Ni<sub>x</sub>Fe<sub>y</sub>)<sub>2</sub>P as both anode and cathode use for overall water splitting demonstrates a nearly 100% Faradaic efficiency. This work may provide significant reference for the produce of low-cost and highly active bifunctional electrocatalysts to realize large-scale commercial applications of overall water splitting.

## Acknowledgments

This work was supported by the National Natural Science Foundation of China (Nos. 51175472 and 51672249), the Zhejiang Outstanding Youth Fund (No. LR19E020004), the Opening Fund of State Key Laboratory of Structural Analysis for Industrial Equipment (Dalian University of Technology) (No. GZ1704) and the Opening Fund of State Key Laboratory of Digital Manufacturing Equipment and Technology (Huazhong University of Science and Technology) (No. DMETKF2018017).

## Appendix A. Supplementary data

Supplementary data to this article can be found online at <https://doi.org/10.1016/j.electacta.2019.07.022>.

## References

- [1] D. Gielen, F. Boshell, D. Saygin, Climate and energy challenges for materials science, *Nat. Mater.* 15 (2016) 117–120.
- [2] X.H. Wang, A.P. Liu, Y. Xing, H.W. Duan, W.Z. Xu, Q. Zhou, H.P. Wu, C. Chen, B.Y. Chen, Three-dimensional graphene biointerface with extremely high sensitivity to single cancer cell monitoring, *Biosens. Bioelectron.* 105 (2018) 22–28.
- [3] C. Xiang, K.M. Papadantonakis, N.S. Lewis, Principles and implementations of electrolysis systems for water splitting, *Mater. Horiz.* 3 (2016) 169–173.
- [4] S.Y. Tee, K.Y. Win, W.S. Teo, L.D. Koh, S. Liu, C.P. Teng, M.Y. Han, Recent progress in energy-driven water splitting, *Adv. Sci.* 4 (2017) 1600337.
- [5] Z. Cao, T. Zhou, W. Xi, Y. Zhao, Bimetal metal-organic frameworks derived Co<sub>0.4</sub>Fe<sub>0.28</sub>P and Co<sub>0.37</sub>Fe<sub>0.26</sub>S nanocubes for enhanced oxygen evolution reaction, *Electrochim. Acta* 263 (2018) 576–584.
- [6] H.P. Wu, S.H. Yu, Z.X. Xu, B.B. Cao, X. Peng, Z. Zhang, G.C. Chai, A.P. Liu, Theoretical and experimental study of reversible and stable wetting states of a hierarchically wrinkled surface tuned by mechanical strain, *Langmuir* 35 (2019) 6870–6877.
- [7] W. Sheng, H.A. Gasteiger, Y. Shao-Horn, Hydrogen oxidation and evolution reaction kinetics on platinum: acid vs alkaline electrolytes, *J. Electrochem. Soc.* 157 (2010) B1529–B1536.
- [8] Y. Lee, J. Suntivich, K.J. May, E.E. Perry, Y. Shao-Horn, Synthesis and activities of rutile IrO<sub>2</sub> and RuO<sub>2</sub> nanoparticles for oxygen evolution in acid and alkaline solutions, *J. Phys. Chem. Lett.* 3 (2012) 399–404.
- [9] F.A. Frame, T.K. Townsend, R.L. Chamousis, E.M. Sabio, T. Dittrich, N.D. Browning, F.E. Osterloh, Photocatalytic water oxidation with non-sensitized IrO<sub>2</sub> nanocrystals under visible and UV light, *J. Am. Chem. Soc.* 133 (2011) 7264–7267.
- [10] J. Zhang, L. Zhao, A. Liu, X. Li, H. Wu, C. Lu, Three-dimensional MoS<sub>2</sub>/rGO hydrogel with extremely high double-layer capacitance as active catalyst for hydrogen evolution reaction, *Electrochim. Acta* 182 (2015) 652–658.
- [11] A. Liu, L. Zhao, J. Zhang, L. Lin, H. Wu, Solvent-assisted oxygen incorporation of vertically aligned MoS<sub>2</sub> ultrathin nanosheets decorated on reduced graphene oxide for improved electrocatalytic hydrogen evolution, *ACS Appl. Mater. Interfaces* 8 (2016) 25210–25218.
- [12] L. Zhao, C. Hong, L. Lin, H. Wu, Y. Su, X. Zhang, A. Liu, Controllable nanoscale engineering of vertically aligned MoS<sub>2</sub> ultrathin nanosheets by nitrogen doping of 3D graphene hydrogel for improved electrocatalytic hydrogen evolution, *Carbon* 116 (2017) 223–231.
- [13] D.R. Cummins, U. Martinez, A. Sherehy, R. Kappera, A. Martinez-Garcia, R.K. Schulz, J. Jasinski, J. Zhang, R.K. Gupta, J. Lou, M. Chhowalla, G. Sumanasekera, A.D. Mohite, M.K. Sunkara, G. Gupta, Efficient hydrogen evolution in transition metal dichalcogenides via a simple one-step hydrazine reaction, *Nat. Commun.* 7 (2016) 11857.
- [14] M.R. Gao, Y.R. Zheng, J. Jiang, S.H. Yu, Pyrite-type nanomaterials for advanced electrocatalysis, *Acc. Chem. Res.* 50 (2017) 2194–2204.
- [15] J.K. Kim, G.D. Park, J.H. Kim, S.K. Park, Y.C. Kang, Rational design and synthesis of extremely efficient macroporous CoSe<sub>2</sub>-CNT composite microspheres for hydrogen evolution reaction, *Small* 13 (2017) 1700068.
- [16] C. Xuan, K. Xia, W. Lei, W. Xia, W. Xiao, L. Chen, H.L. Xin, D. Wang, Composition-dependent electrocatalytic activities of NiFe-based selenides for the oxygen evolution reaction, *Electrochim. Acta* 291 (2018) 64–72.
- [17] Z.Y. Wu, B.C. Hu, P. Wu, H.W. Liang, Z.L. Yu, Y. Lin, Y.R. Zheng, Z. Li, S.H. Yu, Mo<sub>2</sub>C nanoparticles embedded within bacterial cellulose-derived 3D N-doped carbon nanofiber networks for efficient hydrogen evolution, *NPG Asia Mater.* 8 (2016) e288.
- [18] J. Xing, Y. Li, S. Guo, T. Jin, H. Li, Y. Wang, L. Jiao, Molybdenum carbide in-situ embedded into carbon nanosheets as efficient bifunctional electrocatalysts for overall water splitting, *Electrochim. Acta* 298 (2019) 305–312.
- [19] L. Xie, F. Qu, Z. Liu, X. Ren, S. Hao, R. Ge, G. Du, A.M. Asiri, X. Sun, L. Chen, In situ formation of a 3D core/shell structured Ni<sub>3</sub>N@Ni-Bi nanosheet array: an efficient non-noble-metal bifunctional electrocatalyst toward full water splitting under near-neutral conditions, *J. Mater. Chem. A* 5 (2017) 7806–7810.
- [20] M. Chu, L. Wang, X. Li, M. Hou, N. Li, Y. Dong, X. Li, Z. Xie, Y. Lin, W. Cai, C. Zhang, Carbon coated nickel - nickel oxide composites as a highly efficient catalyst for hydrogen evolution reaction in acid medium, *Electrochim. Acta* 264 (2018) 284–291.
- [21] Y. Yang, H. Fei, G. Ruan, C. Xiang, J.M. Tour, Efficient electrocatalytic oxygen evolution on amorphous nickel-cobalt binary oxide nanoporous layers, *ACS Nano* 8 (2014) 9518–9523.
- [22] Y. Wang, Y. Zhang, Z. Liu, C. Xie, S. Feng, D. Liu, M. Shao, S. Wang, Layered double hydroxide nanosheets with multiple vacancies obtained by dry exfoliation as highly efficient oxygen evolution electrocatalysts, *Angew. Chem. Int. Ed.* 56 (2017) 5867–5871.
- [23] Z.-Y. Yu, C.-C. Lang, M.-R. Gao, Y. Chen, Q.-Q. Fu, Y. Duan, S.-H. Yu, Ni-Mo-O nanorod-derived composite catalysts for efficient alkaline water-to-hydrogen conversion via urea electrolysis, *Energy Environ. Sci.* 11 (2018) 1890–1897.
- [24] Z.W. Seh, J. Kibsgaard, C.F. Dickens, I. Chorkendorff, J.K. Nørskov, T.F. Jaramillo, Combining theory and experiment in electrocatalysis: insights into materials design, *Science* 355 (2017) aad4998.
- [25] X. Zou, X. Huang, A. Goswami, R. Silva, B.R. Sathe, E. Mikmekova, T. Asefa, Cobalt-embedded nitrogen-rich carbon nanotubes efficiently catalyze hydrogen evolution reaction at all pH values, *Angew. Chem. Int. Ed. Engl.* 53 (2014) 4372–4376.
- [26] T. Liu, X. Ma, D. Liu, S. Hao, G. Du, Y. Ma, A.M. Asiri, X. Sun, L. Chen, Mn doping of CoP nanosheets array: an efficient electrocatalyst for hydrogen evolution reaction with enhanced activity at all pH values, *ACS Catal.* 7 (2016) 98–102.
- [27] M.Y. Wu, P.F. Da, T. Zhang, J. Mao, H. Liu, T. Ling, Designing hybrid NiP<sub>2</sub>/NiO nanorod arrays for efficient alkaline hydrogen evolution, *ACS Appl. Mater. Interfaces* 10 (2018) 17896–17902.
- [28] J. Chang, Y. Xiao, M. Xiao, J. Ge, C. Liu, W. Xing, Surface oxidized cobalt-phosphide nanorods as an advanced oxygen evolution catalyst in alkaline solution, *ACS Catal.* 5 (2015) 6874–6878.
- [29] M. Ledendecker, S. Krick Calderón, C. Papp, H.P. Steinrück, M. Antonietti, M. Shalom, The synthesis of nanostructured Ni<sub>5</sub>P<sub>4</sub> films and their use as a non-noble bifunctional electrocatalyst for full water splitting, *Angew. Chem. Int. Ed.* 54 (2015) 12361–12365.
- [30] C.G. Read, J.F. Callejas, C.F. Holder, R.E. Schaak, General strategy for the synthesis of transition metal phosphide films for electrocatalytic hydrogen and oxygen evolution, *ACS Appl. Mater. Interfaces* 8 (2016) 12798–12803.
- [31] J. Kibsgaard, C. Tsai, K. Chan, J.D. Benck, J.K. Nørskov, F. Abild-Pedersen, T.F. Jaramillo, Designing an improved transition metal phosphide catalyst for hydrogen evolution using experimental and theoretical trends, *Energy Environ. Sci.* 8 (2015) 3022–3029.

- [32] J. Duan, S. Chen, A. Vasileff, S.Z. Qiao, Anion and cation modulation in metal compounds for bifunctional overall water splitting, *ACS Nano* 10 (2016) 8738–8745.
- [33] C. Guan, W. Xiao, H. Wu, X. Liu, W. Zang, H. Zhang, J. Ding, Y.P. Feng, S.J. Pennycook, J. Wang, Hollow Mo-doped CoP nanoarrays for efficient overall water splitting, *Nano Energy* 48 (2018) 73–80.
- [34] D. Liu, S. Ding, C. Wu, W. Gan, C. Wang, D. Cao, Z.u. Rehman, Y. Sang, S. Chen, X. Zheng, Y. Wang, B. Ge, L. Song, Synergistic effect of an atomically dual-metal doped catalyst for highly efficient oxygen evolution, *J. Mater. Chem. A* 6 (2018) 6840–6846.
- [35] C. Xuan, J. Wang, W. Xia, Z. Peng, Z. Wu, W. Lei, K. Xia, H.L. Xin, D. Wang, Porous structured Ni–Fe–P nanocubes derived from a prussian blue analogue as an electrocatalyst for efficient overall water splitting, *ACS Appl. Mater. Interfaces* 9 (2017) 26134–26142.
- [36] S.H. Ahn, A. Manthiram, Direct growth of ternary Ni–Fe–P porous nanorods onto nickel foam as a highly active, robust bi-functional electrocatalyst for overall water splitting, *J. Mater. Chem. A* 5 (2017) 2496–2503.
- [37] B. Zhang, Y.H. Lui, H. Ni, S. Hu, Bimetallic ( $\text{Fe} \times \text{Ni} (1-x) \text{ } 2 \text{ P}$ ) nanoarrays as exceptionally efficient electrocatalysts for oxygen evolution in alkaline and neutral media, *Nano Energy* 38 (2017) 553–560.
- [38] C. Xuan, Z. Peng, K. Xia, J. Wang, W. Xiao, W. Lei, M. Gong, T. Huang, D. Wang, Self-supported ternary Ni–Fe–P nanosheets derived from metal–organic frameworks as efficient overall water splitting electrocatalysts, *Electrochim. Acta* 258 (2017) 423–432.
- [39] L. Zhou, M. Shao, J. Li, S. Jiang, M. Wei, X. Duan, Two-dimensional ultrathin arrays of CoP: electronic modulation toward high performance overall water splitting, *Nano Energy* 41 (2017) 583–590.
- [40] S.T. Oyama, T. Gott, H. Zhao, Y.-K. Lee, Transition metal phosphide hydroprocessing catalysts: a review, *Catal. Today* 143 (2009) 94–107.
- [41] E.J. Popczun, J.R. McKone, C.G. Read, A.J. Biacchi, A.M. Wiltrot, N.S. Lewis, R.E. Schaak, Nanostructured nickel phosphide as an electrocatalyst for the hydrogen evolution reaction, *J. Am. Chem. Soc.* 135 (2013) 9267–9270.
- [42] Z. Pu, Q. Liu, C. Tang, A.M. Asiri, X. Sun, Ni<sub>2</sub>P nanoparticle films supported on a Ti plate as an efficient hydrogen evolution cathode, *Nanoscale* 6 (2014) 11031–11034.
- [43] H. Du, L. Xia, S. Zhu, F. Qu, F. Qu, Al-Doped Ni<sub>2</sub>P nanosheet array: a superior and durable electrocatalyst for alkaline hydrogen evolution, *Chem. Commun.* 54 (2018) 2894–2897.
- [44] X. Zhang, S. Zhu, L. Xia, C. Si, F. Qu, F. Qu, Ni(OH)<sub>2</sub>–Fe<sub>2</sub>P hybrid nanoarray for alkaline hydrogen evolution reaction with superior activity, *Chem. Commun.* 54 (2018) 1201–1204.
- [45] X. Ren, W. Wang, R. Ge, S. Hao, F. Qu, G. Du, A.M. Asiri, Q. Wei, L. Chen, X. Sun, An amorphous FeMo<sub>34</sub> nanorod array toward efficient hydrogen evolution electrocatalysis under neutral conditions, *Chem. Commun.* 53 (2017) 9000–9003.
- [46] P. Xiao, W. Chen, X. Wang, A review of phosphide-based materials for electrocatalytic hydrogen evolution, *Adv. Energy Mater.* 5 (2015), 1500985.
- [47] J. Li, M. Yan, X. Zhou, Z.Q. Huang, Z. Xia, C.R. Chang, Y. Ma, Y. Qu, Mechanistic insights on ternary Ni<sub>2-x</sub>Co<sub>x</sub>P for hydrogen evolution and their hybrids with graphene as highly efficient and robust catalysts for overall water splitting, *Adv. Funct. Mater.* 26 (2016) 6785–6796.
- [48] W. Chen, I.K. Mishra, Z. Qin, L. Yu, H. Zhou, J. Sun, F. Zhang, S. Chen, G.E. Wenya, Y. Yu, Z.M. Wang, H.-Z. Song, Z. Ren, Nickel phosphide based hydrogen producing catalyst with low overpotential and stability at high current density, *Electrochim. Acta* 299 (2019) 756–761.
- [49] X. Xiao, L. Tao, M. Li, X. Lv, D. Huang, X. Jiang, H. Pan, M. Wang, Y. Shen, Electronic modulation of transition metal phosphide via doping as efficient and pH-universal electrocatalysts for hydrogen evolution reaction, *Chem. Sci.* 9 (2018) 1970–1975.
- [50] Y.P. Zhu, Y.P. Liu, T.-Z. Ren, Z.-Y. Yuan, Self-supported cobalt phosphide mesoporous nanorod arrays: a flexible and bifunctional electrode for highly active electrocatalytic water reduction and oxidation, *Adv. Funct. Mater.* 25 (2015) 7337–7347.
- [51] A. Sivanantham, P. Ganesan, S. Shanmugam, Hierarchical NiCo<sub>2</sub>S<sub>4</sub> nanowire arrays supported on Ni foam: an efficient and durable bifunctional electrocatalyst for oxygen and hydrogen evolution reactions, *Adv. Funct. Mater.* 26 (2016) 4661–4672.
- [52] M.W. Louie, A.T. Bell, An investigation of thin-film Ni–Fe oxide catalysts for the electrochemical evolution of oxygen, *J. Am. Chem. Soc.* 135 (2013) 12329–12337.